

Cell Segmentation and Tracking using CNN-Based Distance Predictions and a Graph-Based Matching Strategy

Tim Scherr¹, Katharina Löffler^{1,2}, Moritz Böhlend¹, Ralf Mikut¹

¹ Institute for Automation and Applied Informatics, Karlsruhe Institute of Technology, 76344 Eggenstein-Leopoldshafen, Germany

² Institute of Biological and Chemical Systems - Biological Information Processing, Karlsruhe Institute of Technology, 76344 Eggenstein-Leopoldshafen, Germany

Corresponding author: Tim Scherr (e-mail: tim.scherr@kit.edu).

This work has been supported by the Helmholtz Association in the program BioInterfaces in Technology and Medicine (BIFTM), and the Helmholtz Information & Data Science School for Health (HIDSS4Health).

ABSTRACT

The accurate segmentation and tracking of cells in microscopy image sequences is an important task in biomedical research, e.g., for studying the development of tissues, organs or entire organisms. However, the segmentation of touching cells in images with a low signal-to-noise-ratio is still a challenging problem. In this paper, we present a method for the segmentation of touching cells in microscopy images. By using a novel representation of cell borders, inspired by distance maps, our method is capable to utilize not only touching cells but also close cells in the training process. Furthermore, this representation is notably robust to annotation errors and shows promising results for the segmentation of microscopy images containing in the training data underrepresented or not included cell types. For the prediction of the proposed neighbor distances, an adapted U-Net convolutional neural network (CNN) with two decoder paths is used. In addition, we adapt a graph-based cell tracking algorithm to evaluate our proposed method on the task of cell tracking. The adapted tracking algorithm includes a movement estimation in the cost function to re-link tracks with missing segmentation masks over short time spans. Our combined tracking by detection method has proven its potential in the IEEE ISBI 2020 Cell Tracking Challenge (<http://celltrackingchallenge.net/>) where we achieved as team KIT-Sch-GE multiple top three rankings including two top performances using a single segmentation model for the diverse data sets.

1 Introduction

State-of-the-art microscopy imaging techniques such as light-sheet fluorescence microscopy imaging enable, for instance, to investigate cell dynamics with single-cell resolution [1, 2]. This allows to study cell migration and proliferation in tissue development and organ formation at early embryonic stages. Establishing the required complete lineage of each cell, however, requires a virtually error-free segmentation and tracking of individual cells over time [2, 3]. A manual data analysis is unfeasible, due to the large amount of data acquired with modern imaging techniques. In addition, low-resolution objects are very difficult to detect even for human experts. Deep learning-based segmentation methods have proven to outperform traditional methods even on very diverse 2D data sets [4]. However, state-of-the-art cell tracking methods often still need a time-consuming manual cell track curation, e.g., using EmbryoMiner [5] or the Massive Multi-view Tracker (MaMuT) [6]. Especially for low signal-to-noise ratio and 3D data, further method development is required for both cell segmentation and cell tracking [7].

Traditional segmentation methods, such as TWANG for the segmentation of roundish objects [9], are often designed for a specific application. These methods commonly consist of sophisticated combinations of pre-processing filters, e.g., Gaussian or median filters, and segmentation operations, e.g., a region adaptive thresholding followed by a watershed transform [8]. Thus, traditional methods need to be carefully adapted to the cell type and imaging conditions in order to reach a reasonable segmentation quality. Therefore, expert knowledge is needed. In contrast, deep learning-based segmentation methods shift the expert knowledge needed to the model design and to the training process. Thus, less expert knowledge is needed for the application of a trained model and to fine-tune the post-processing which is often

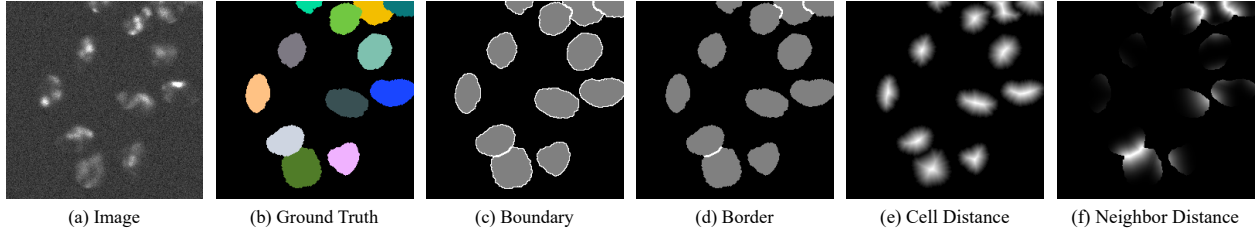


Figure 1: Training data representations for the training of deep learning models. Boundaries (c) and borders (d) can be used to split touching cells. Many training data sets contain only few touching cells resulting in few training samples for borders and boundaries between cells. The combination of cell distance labels (e) with neighbor distance labels (f) is aimed to solve this problem since models can also learn from close cells. The image (a) shows a crop of the simulated Cell Tracking Challenge data set Fluo-N2DH-SIM+ [7, 8].

kept very simple. To improve the generalization ability of a trained deep learning model, a preferably diverse and large annotated data set is needed. This fact is especially problematic when dealing with touching cells since this case is usually underrepresented in training data sets. Therefore, models for cell boundary or border prediction (see Fig. 1) are often not able to handle touching cells well. The result are merged cells, due to gaps in predicted cell boundaries and borders between touching cells [10, 11]. To overcome this problem, several approaches have been proposed. In [10], models are trained to predict adapted thicker borders and smaller cells, which can decrease the amount of merged cells. [11] utilizes a new gap class and adapted borders with J regularization. [12] combines distance transforms for single cell nuclei with discrete boundaries. A center vector encoding which is aimed to be more robust to label inconsistencies is proposed in [13], whereas in [14], horizontal and vertical gradient maps are used. To improve the generalization ability of a model for cell types with only few or no annotated images, a generative adversarial network-based image style transfer to generate augmented training samples of that cell types has been used in [15]. An advantage of border-based approaches is that a deep learning model is enforced to focus on in the training data underrepresented touching cells. However, border-based approaches still have the shortcoming that only touching cells can be used to train the border prediction.

Although deep learning methods have been successfully applied to multi object tracking on natural images [16, 17], there are only few deep learning approaches for cell tracking [18, 19]. In [18], cells are simultaneously segmented and tracked by combining a recurrent hourglass network with a pixel-wise metric embedding learning. [19] proposes a particle-filter-based motion model in combination with a CNN-based observation model. However, cell tracking is still dominated by traditional tracking approaches [7, 20]. One reason is the lack of high quality annotations as provided in natural image tracking benchmarks [21, 22, 23]. Thus, training data are often not available. Another aspect that complicates the task of cell tracking are cell death and division events, which do not occur in natural image tracking data. Therefore, traditional tracking algorithms with comparably few parameters and explicit modeling of cell division events still dominate cell tracking benchmarks [7]. The comparison of cell tracking algorithms in [7] shows a majority of tracking approaches use an adapted version of nearest neighbors, a graph-based linking or multi hypothesis tracking. In [20], the Viterbi algorithm is applied to solve the track linking problem. A joint model for segmentation and tracking is proposed in [24] where model parameters are learned based on Bayes risk minimization.

In this paper, we propose a novel representation of cell borders, the neighbor distances, to solve the challenging problem of segmenting touching cells of various types in the absence of large training data sets. Thus far, problems of border prediction approaches are the sensitivity to annotation inconsistencies, and that only touching cells provide border information in the training. The neighbor distances are aimed to be less sensitive to annotation inconsistencies, and enable to learn also from close cells. This additional information in the training process results in a more robust border prediction. For the cell tracking, we adapt a minimum-cost flow algorithm to include object movement estimation. In addition, our formulation is able to link fragmented tracks due to missing segmentation masks over short time periods. Section 2 describes the distance prediction segmentation method and the cell tracking algorithm. Data sets and evaluation measures used for benchmarking are described in Section 3. In Section 4, experiments and results are presented and discussed. Section 5 concludes this work.

2 Methods

In this section, we describe our proposed distance prediction segmentation method and the subsequent graph-based cell tracking in detail.

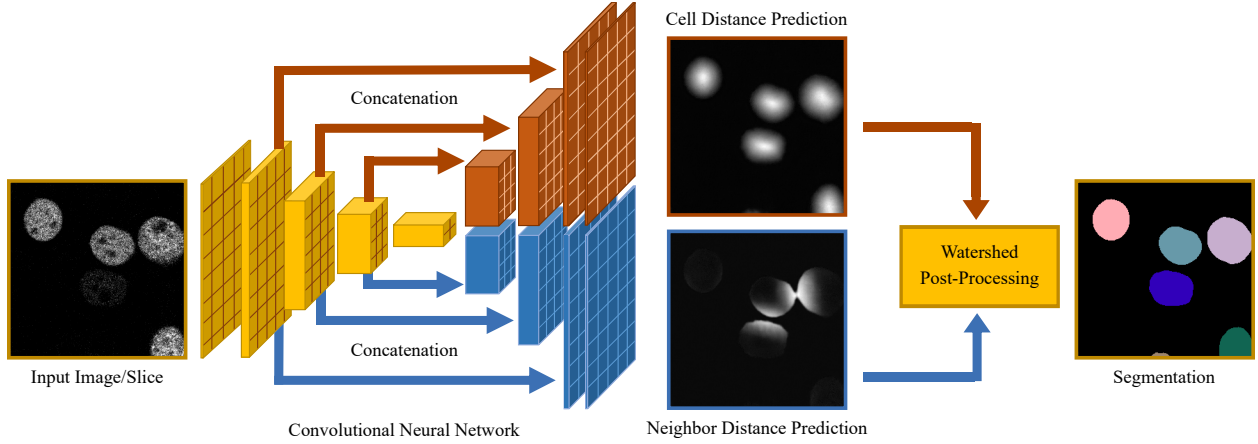


Figure 2: Overview of the proposed segmentation method using distance predictions (adapted from [12]). The convolutional neural network consists of a single decoder that is connected with both decoder paths. The network is trained to predict cell distances and neighbor distances that are used for the watershed-based post-processing. The input image shows a crop of the Cell Tracking Challenge data set Fluo-N2DH-GOWT1 [7, 8].

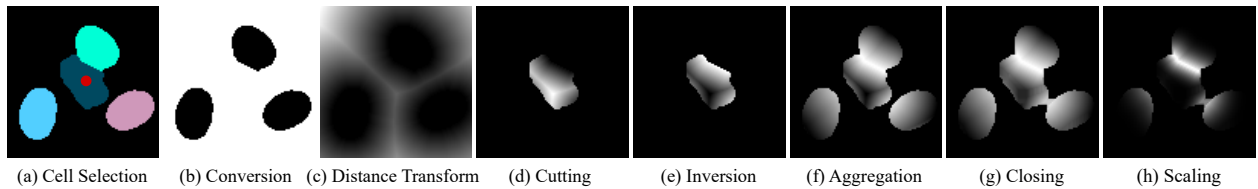


Figure 3: Main steps of the neighbor distance creation. After the selection of a cell (a), indicated with red, the selected cell and the background are converted to foreground (white in b) while the other cells are converted to background (black in b). Then, the distance transform is calculated (c), cut to the cell region and normalized (d). After inversion (e), the steps are repeated for the remaining cells (f). Finally, the grayscale closed neighbor distances (g) are scaled (h). Shown is a crop of the Broad Bioimage Benchmark Collection data set BBBC039v1 [25].

2.1 Distance Prediction Segmentation

For cell segmentation, we train a deep learning model to predict cells and cell borders, followed by a post-processing with a seed extraction and a seed-based watershed segmentation. A key for the successful application of supervised deep learning methods in the absence of large training data sets is to introduce representations that allow to use as much information as possible. Thus, instead of discrete cell boundary (Fig. 1c) and cell border representations (Fig. 1d), we combine cell distances (Fig. 1e, [12]) with novel neighbor distances (Fig. 1f). These representations allow incorporating the regional information not only from touching cells but also from close cells resulting in more robust deep learning models. A segmentation network based on the U-Net architecture [26], modified similar to [12], is utilized as the backbone of the method. An overview of the proposed method provides Fig. 2.

2.1.1 Cell and Neighbor Distances

To generate cell distances, as shown in Fig. 1, from ground truth data, the Euclidean distance transform is calculated for each cell independently, treating adjacent cells as background, and normalized to the range $[0, 1]$. Thus, each pixel of a cell represents the distance to the nearest pixel not belonging to this cell. The cell distance prediction alone is sufficient to obtain seeds for the post-processing. However, a precondition is that the convolutional neural network has learned to deal with cell distances of touching cells. By combining cell distances with the novel neighbor distances the erroneous merging of touching cells is prevented.

In the neighbor distances, each pixel of a cell represents the distance to the nearest pixel of another cell. Fig. 3 shows the generation of the neighbor distances, which are normalized to the range $[0, 1]$, using a background-foreground conversion step (Fig. 3b) and the Euclidean distance transform (Fig. 3c). The distance transform is cut to the cell size and normalized (Fig. 3d) followed by an inversion (Fig. 3e). The normalization is required to suppress neighbor

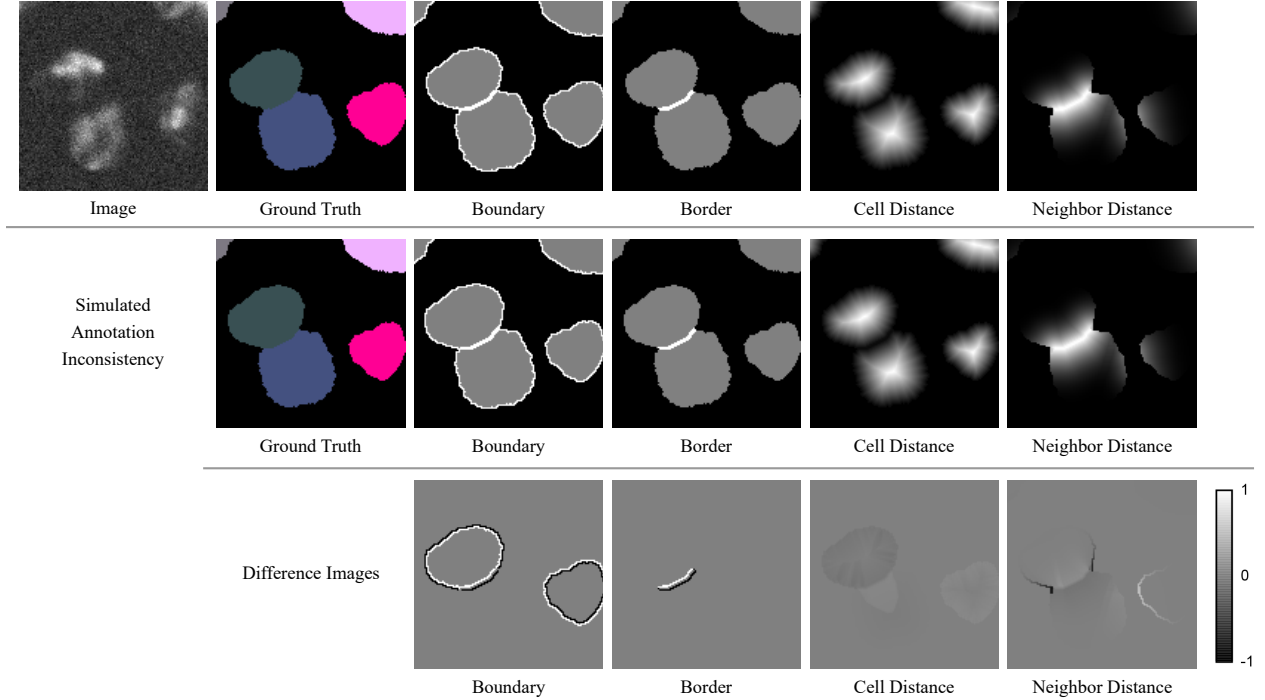


Figure 4: Robustness of training data representations to annotation inconsistencies. Small changes in the ground truth, simulated with morphological erosions and dilations, result in different boundaries and borders (first and second row). The difference images between the first row and the second row show that the changes for the distance labels are smoother. Shown is a closer look to the image in Fig. 1.

distances for cells without close neighbors. To further reduce the erroneously merging of cells, gaps between close cells are closed by applying a grayscale closing (Fig. 3g). Finally, to get a steeper decline within cells, a scaling is applied by taking the closed neighbor distances (Fig. 3g) to the power of three (Fig. 3h). This confines the neighbor distances to the outer cell area and therefore eases the seed extraction in the post-processing.

Fig. 4 shows that the neighbor distances are more robust to annotation inconsistencies than boundaries and borders, i.e., a cell was morphologically eroded and another cell dilated resulting in masks that only differ in single pixels. The location of the discrete boundaries and borders change, meaning that a prediction of the initial border is considered incorrect and penalized in the training. This makes it difficult to train models well on small data sets. In contrast, the proposed continuous neighbor distance shows a smooth change. Therefore, the influence of annotation inconsistencies on the training process is reduced resulting in a more robust training.

Another advantage of the neighbor distances is that they also provide information in the training process when cells are close but do not touch. This can be seen in Fig. 3h (bottom right cell and bottom left cell) and is especially advantageous for training data sets with few touching cells providing only little border information in the training process.

2.1.2 Architecture and Training Settings

The architecture used is based on the U-Net architecture [26]. However, instead of a single decoder path, two parallel decoder paths are used allowing each decoder path to focus on features related to the desired output. In addition, the feature detection in the shared encoder branch of the network is trained using backpropagated information from both decoder branches. The maximum pooling layers are replaced with 2D convolutional layers with stride 2 and kernel size 3. Additionally, batch normalization layers are added. The number of feature maps is doubled from 64 feature maps to a maximum of 1024 in the encoder path and halved in each decoder path correspondingly. To avoid the need of cropping before concatenation, zero padding is applied in the convolutional layers to keep the feature map size consistent. The rectified linear unit activation function is used within the network and a linear activation for the output layers. Fig. 2 provides an overview of the architecture, i.e., convolutional and downsampling layers are summarized into blocks.

Models are trained with a batch size of 8 using the Adam optimizer [27] and the learning rate is initialized with 8×10^{-4} . After 12 subsequent epochs without validation loss improvement, the learning rate is multiplied by 0.25

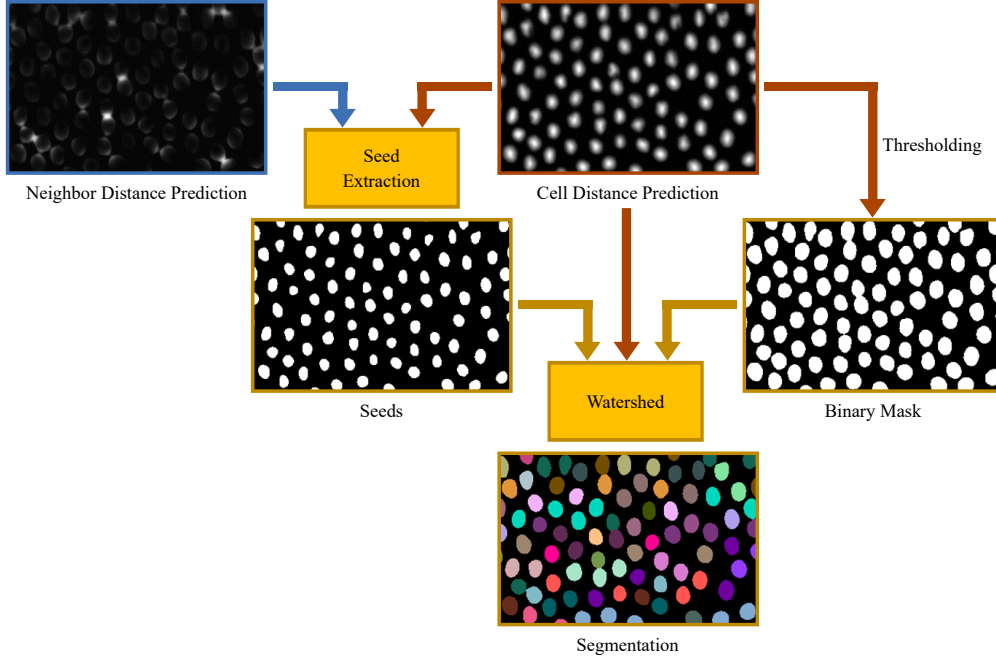


Figure 5: Overview of the watershed post-processing for segmentation. The post-processing consists of a threshold-based seed extraction and mask creation, and a watershed. The predictions show a 2D crop of the Cell Tracking Challenge data set Fluo-N3DL-TRIC [7, 8].

till a minimum learning rate of 6×10^{-5} is reached. The training is stopped when 28 subsequent epochs without improvement occurred or a maximum amount of total epochs is reached. To learn the cell distances and the neighbor distances, PyTorch’s SmoothL1Loss is used and both losses are added. During training the augmentations flipping, scaling, rotation, contrast changing, blurring, and noise adding are applied. We recommend to min-max normalize the training images into the range $[-1, 1]$ and to apply a cropping if needed, e.g., due to VRAM restrictions.

2.1.3 Inference

For inference, each frame of a time series is min-max normalized independently into the range $[-1, 1]$, whereas the whole volume is normalized for 3D data. The normalized data are processed frame-by-frame with 3D data being processed slice-wise (we refer to the slice dimension as xy -dimension). The CNN model inputs are zero-padded if necessary.

2.1.4 Watershed Post-Processing

Fig. 5 shows the main steps of the post-processing. The cell distance predictions and the neighbor distance predictions are smoothed with a Gaussian kernel of the same dimensionality as the image. Then, the region to flood with a seed-based watershed is extracted from the smoothed cell distance prediction by applying a threshold. To obtain the seeds, the smoothed and squared neighbor distance prediction is subtracted from the cell prediction and the result is thresholded. Depending on the cell size, the squaring can be omitted or replaced by an even steeper function. Seeds with an area smaller than 3 px^2 are removed.

For 3D data, detected merged cells in z -direction can be split by increasing the seed extraction threshold till multiple seeds are found for that cell. For the detection of merged cells, a priori knowledge about cell volumes can be used or a cell volume outlier detection.

Inspired by the Dual U-Net architecture [12], we first attempted to enforce the convolutional neural network to predict an additional seed output from the cell distances and the neighbor distances. However, our traditional post-processing provided better results in tests and enables a fine-tuning to in the training unseen cell types. In addition, it simplifies the architecture and the training process.

2.2 Tracking

Cell tracking aims to reconstruct the lineage of cells, by linking related cells over time. This linking task is trivial in case of low cell density, error-free segmentation, and high temporal resolution resulting in negligible cell movements between adjacent frames. However, especially for low signal-to-noise-ratio images with touching and dividing cells, fragmented tracks can occur. To re-link fragmented tracks, we match tracks without assigned cells for small time spans and add a coarse position estimation to the cost function. The proposed algorithm is capable of tracking all segmented cells in an image sequence as well as tracking only a subset, e.g., a selection of manually marked cells in the first frame.

2.2.1 Initialization

The tracking algorithm traverses the time steps forward. A track is initialized for each segmented object in the first frame. For data sets with marked objects in the first frame, tracks are only initialized for marked objects. It is assumed that the object movement between successive frames is small compared to the overall image size. Therefore, for each tracked object a rectangular shaped region of interest (ROI) is defined as a search space for the same object in the next frame. The initial center of each ROI is set to the median position calculated from the first assigned segmentation mask of each track.

2.2.2 Movement Estimation & Graph-Based Matching Strategy

The tracking step consists of a movement estimation followed by a graph-based matching strategy. To estimate the object movement between successive frames, a displacement between successive images I_t and I_{t+1} is estimated. Therefore, for each tracked object a cross-correlation is computed between its ROI at I_t and I_{t+1} . Based on the estimated displacements, the ROIs at time step $t + 1$ are adapted.

To re-link tracks with missing segmentation masks for short time spans, all tracks with no successors and their last assigned segmentation mask within time span $\{t - \Delta t, \dots, t\}$ are considered active. Next, for each active track a set of potential matching candidates is selected based on its ROI at time step $t + 1$. Active tracks and potential matching candidates are matched by using an adapted version of the coupled minimum-cost flow algorithm proposed by [28]. An overview of the adapted graph structure is shown in Fig. 6. The matching algorithm minimizes the overall matching cost between active tracks and potential matching candidates subject to a set of constraints modeling flow, appearance/disappearance of objects, and splitting/merging of objects. The by [28] proposed algorithm has been adapted as follows: The appearance cost of objects are set to 0, as spurious tracks will be filtered out by the subsequent post-processing. This appears to be advantageous in scenarios with the objective to track only a few selected objects. The disappearance cost is set to the length of the largest edge of the ROI instead of using appearance-based features. Therefore, tracks with missing segmentation masks can be assigned to the disappearance node as well. The merging node proposed in [28] is removed, as it only models the merging of two objects per time step. The matching cost $c_{s,n}$ between track s and potential matching candidate n is adapted to:

$$c_{s,n} = \|\hat{p}_{t+1}^s - p_{t+1}^n\|_2, \quad (1)$$

where \hat{p}_{t+1}^s is the estimated position of the tracked object s at time $t + 1$ and p_{t+1}^n the position of the potential matching candidate. The estimated position \hat{p}_{t+1}^s is given by:

$$\hat{p}_{t+1}^s = p_t^s + d^s, \quad (2)$$

where d^s is the estimated displacement of the ROI of track s between time step t and $t + 1$. p_t^s is the position of the tracked object at time step t . The cost of split events are computed based on the size and position of the tracked object s and its potential successor candidates n and k :

$$c_{s,(n,k)} = \begin{cases} \|\hat{p}_{t+1}^s - \frac{1}{2}(p_{t+1}^n + p_{t+1}^k)\|_2 & \text{if } C_s = 1, \\ \rho & \text{else,} \end{cases} \quad (3)$$

where $c_{s,(n,k)}$ are the split costs and C_s the split condition. In practice, we set ρ to ten times the disappearance cost. The split condition C_s is defined as:

$$C_s = \begin{cases} 1 & \text{if } \frac{V_{t+1}^n}{V_{t+1}^k} > \alpha, \frac{V_{t+1}^n + V_{t+1}^k}{V_{t_{last}}^s} < \beta, \|p_{t+1}^n - p_{t+1}^k\|_2 < \gamma, \\ 0 & \text{else,} \end{cases} \quad (4)$$

with $V_{t+1}^k \geq V_{t+1}^n$. V_{t+1}^n , V_{t+1}^k and $V_{t_{last}}^s$ are the areas/volumes of the segmentation masks of successor candidates n and k , and of the last assigned object to the track s at time step t_{last} , respectively. α , β and γ are hyper-parameters.

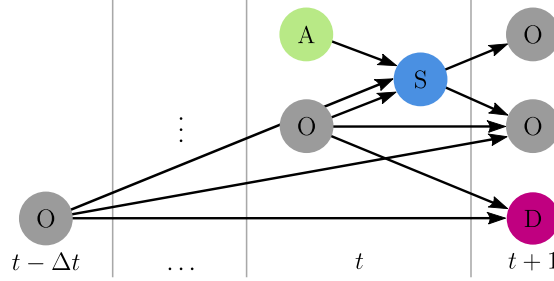


Figure 6: Graph-based matching algorithm adapted from [28]. Gray nodes are segmented objects (O). The segmented objects from $\{t - \Delta t, \dots, t\}$ are the last matched objects of all active tracks, whereas the segmented objects of $t + 1$ are not matched to tracks yet. The green node models the appearance of objects (A), the pink node the disappearance of objects (D), and the blue node cell divisions (S).

A possible parametrization of those hyper-parameters is provided in Section 4.5. The split condition ensures that successors should be of similar size, have a combined area/volume similar to the area/volume of the predecessor object, and should be reasonably close to each other.

Each active track is only linked to segmented objects overlapping with its ROI, reducing the number of edges in the graph. As all active tracks are added to the graph and not only segmented objects between successive time steps, tracks with missing segmentation masks for short time spans can be linked. The missing segmentation masks are added by placing masks at the linearly interpolated positions between t_{last} and $t + 1$. For data sets which aim to track all segmented objects, each non-matched object at time step $t + 1$ is initialized as a new track.

2.2.3 Post-Processing

In the post-processing step, trajectories of length one without any predecessor and successors are removed.

3 Data Sets and Evaluation Metrics

Our proposed segmentation method is evaluated on the data set BBBC039v1 of the Broad Bioimage Benchmark Collection [25] and on Cell Tracking Challenge data sets [7, 8].

3.1 BBBC039 Data Set

The data set BBBC039v1 consists of 200 annotated images of U2OS cell nuclei captured with fluorescence microscopy. The images show many touching nuclei. After visual inspection, we decided to exclude two images from the training set and an image from the test set due to missing nuclei or questionable annotations. In order to make the data set more challenging, we reduced the training set to 25 images and the validation set to 12 images. Ground truth objects with an area smaller than 56 px^2 are removed in the 49 test images since we regard them as annotation errors. After that, a border correction which removes all nuclei appearing only in the border region (10 px) is applied. This enables a better comparability of results since border objects are often not annotated consistently.

3.2 Cell Tracking Challenge Data Sets

The Cell Tracking Challenge data are split into training sets with publicly available ground truths, and challenge sets. Thereby, the annotated training sets consist of two different subsets. The provided annotations consist of gold truth (GT) instance segmentation masks, interlinked GT cell seeds for cell detection and tracking, and computer-generated instance segmentation masks, referred to as silver truth (ST). The ST annotations, computed from a majority vote of submitted algorithms of former challenge participants, are only available for a few data sets and can include segmentation errors. However, the GT segmentation masks not necessarily include all cells in a frame. To compare segmentation methods,

we use training data from one subset and evaluate on the other subset. In our challenge submission, we used data from both subsets for the training.

Segmentation Training Data Set

Since only some provided GT images are fully annotated and the ST images may include segmentation errors, we manually selected GT images where all cells in a frame are annotated, and ST images that do not show obvious segmentation errors. 27 GT images of the data set BF-C2DL-HSC (Mouse hematopoietic stem cells showing many cell divisions), 15 GT images of the data set BF-C2DL-MuSC (flexible Mouse muscle stem cells), 16 ST images of the data set Fluo-N2DL-HeLa (HeLa cells), and 3 GT slices of the 3D data set Fluo-N3DH-CE (low signal-to-noise-ratio *C.elegans* developing embryo) fulfilled our requirements. The training data set will be referred to as CTC training set and consists of 268 crops of size $256 \text{ px} \times 256 \text{ px}$ which includes 52 crops used for validation. In contrast to the BBBC039v1 data set, the images contain less touching cells.

3.3 Evaluation Measures

For the evaluation of the instance segmentation results of the data set BBBC039v1, we use the mean average precision at different intersection over union thresholds P_{IoU} with a minimum threshold of 0.5 [4]. This metric penalizes errors at pixel level (shape) and object level (adding, splitting, missing and merging of cells). Any imprecise segmentation results in a decrease in P_{IoU} , where a score of 0 indicates a completely wrong segmentation and 1 a perfect segmentation. The scores are calculated for each image and then averaged.

In addition, we use the performance measures of the Cell Tracking Challenge to evaluate the corresponding data: the normalized acyclic oriented graph matching measure for detection DET to evaluate object level segmentation errors [29], the on the Jaccard similarity index based measure SEG to evaluate pixel level segmentation errors, and the normalized acyclic oriented graph matching measure TRA to evaluate the tracking [29]. The overall performances for the Cell Segmentation Benchmark (CSB) and Cell Tracking Benchmark (CTB) are calculated as follows:

$$OP_{CSB} = 0.5 \cdot (DET + SEG), \quad (5)$$

$$OP_{CTB} = 0.5 \cdot (SEG + TRA). \quad (6)$$

4 Experiments and Results

4.1 Experimental Environment

We performed the experiments using a system with two NVIDIA TITAN RTX GPUs, Ubuntu 18.04, and a Intel Core i9-9900K CPU with 32 GB RAM. The methods are implemented in Python and PyTorch is used as deep learning framework. For the Cell Tracking Challenge data, Linux executables are available on the challenge website.

4.2 Compared Segmentation Methods

The proposed distance prediction segmentation method is trained with the settings described in Section 2 for a maximum of 200 epochs. If not stated otherwise, the post-processing thresholds for the binary mask creation and for the seed extraction are fixed to 0.09 and 0.5, and the standard deviation of the Gaussian smoothing kernel is fixed to 1.5 in xy -direction and to 0.5 in z -direction (3D-data only).

Boundary and border prediction methods (Fig. 1c, Fig. 1d) are trained with the same settings using only a single decoder path. Instead of the linear activation in the output layer and the SmoothL1Loss, the softmax activation is applied to the three-channel output (background, cell, border/boundary). In addition, we use a method with adapted borders as proposed in [10] and two decoder paths. One decoder path is trained to predict binary cell masks (sigmoid activation), the other to predict eroded cells and adapted borders (three channels background, cell and border with softmax activation) for a more robust seed detection. A weighted sum of Dice loss and cross entropy loss is used to train these methods. In the post-processing, the binary masks (threshold 0.5 for the adapted border method, $\arg \max$ of the cell channel for the other methods) and seeds ($\text{cell} * (1 - \text{border/boundary}) > 0.5$) are extracted for a watershed segmentation. Similar to our proposed method, seeds with an area smaller than 3 px^2 are removed.

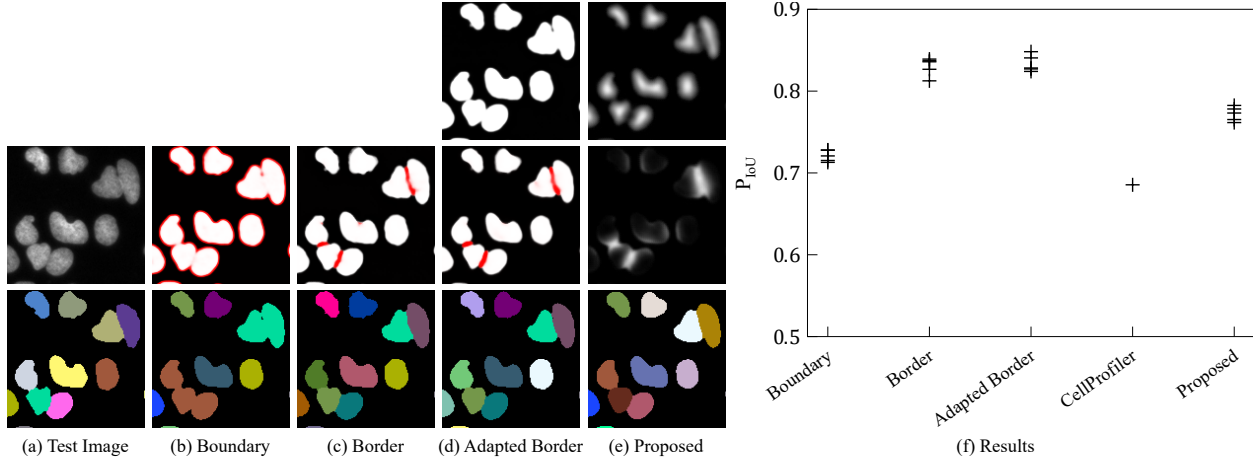


Figure 7: Segmentation results on the BBBC039v1 test set using the reduced BBBC039v1 training set. Shown are raw predictions and segmentations of a $140 \text{ px} \times 140 \text{ px}$ test image crop (a-e). For multi-channel outputs, the boundary/border prediction is visualized in red and the cell/seed channel in white. For comparison purposes, the predictions of a method’s median model are shown (b-e). The plot on the right shows the results on the test set (f).

For each method, five models are trained. This allows to evaluate the robustness of the training. For the BBBC039v1 data set, also a comparison with the provided CellProfiler segmentation pipeline is performed [30].

4.3 Training Data with a Single Cell Type

The first application case is the segmentation of touching cell nuclei of a single type using the reduced BBBC039v1 training set showing many touching nuclei. The methods are evaluated on the BBBC039v1 test set. As for the test set, we applied the border correction and removed small objects also on the results of the compared methods.

Fig. 7 shows that the (adapted) borders can be learned well and outperform the other methods. In the boundary method, the boundaries are sometimes not closed in-between cells resulting in the merging of cells (Fig. 7b). The proposed cell and neighbor distances are learned well (Fig. 7e). However in rare cases additional splits occur (median 1.08% splits) preventing to reach the adapted border scores (median 0.30% splits). The CellProfiler segmentation is outperformed by all deep learning models.

4.4 Training Data with Various Cell Types

More realistic is the case that no or only a few annotated images for the cell type to segment are available since annotating images is time consuming. In addition, a goal may be to have a segmentation method which can segment multiple cell types including also types which do not show many touching cells. This makes the training of borders more difficult. Thus, we trained the compared methods on the CTC training set and evaluated them for multiple cell types.

4.4.1 BBBC039

Fig. 8 shows the segmentation results on the BBBC039v1 test set. As for the test set, we applied the border correction and removed small objects also on the results of the methods. Compared to the previous experiment (see Fig. 7), our proposed method has only a small decline in performance and provides the best segmentation, while the other deep learning-based methods drop in performance.

Especially the border method is not able to predict adequate borders anymore. The thicker adapted borders with the cell seed channel, which is trained on eroded cells, are more robust. However, the proposed neighbor distances utilize also information from close cells in the training process and therefore provide the best results. Though not trained on images of this cell type, our proposed method outperforms the data set specific CellProfiler pipeline.

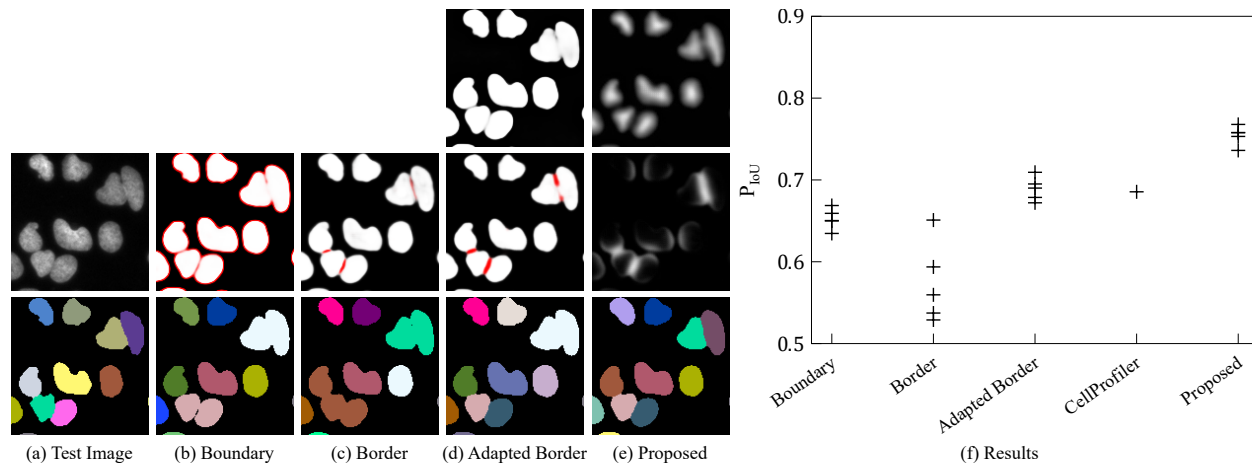


Figure 8: Segmentation results on the BBBC039v1 test set using the CTC training set. Shown are raw predictions and segmentations of a $140 \text{ px} \times 140 \text{ px}$ test image crop (a-e). For multi-channel outputs, the boundary/border prediction is visualized in red and the cell/seed channel in white. For comparison purposes, the predictions of a method’s median model are shown (b-e). The plot on the right shows the results on the test set (f).

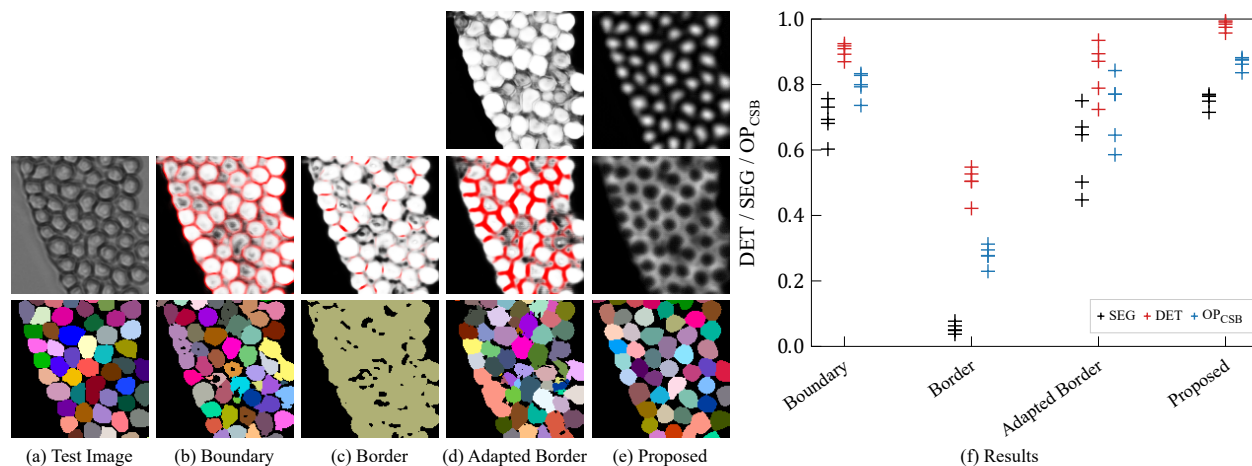


Figure 9: Segmentation results on the BF-C2DL-HSC test set using the CTC training set. Shown are raw predictions and segmentations of a $140 \text{ px} \times 140 \text{ px}$ test image crop (a-e). For multi-channel outputs, the boundary/border prediction is visualized in red and the cell/seed channel in white. For comparison purposes, the predictions of a method’s median OP_{CSB} model are shown (b-e). The plot on the right shows the results on the test set (f).

4.4.2 BF-C2DL-HSC

The segmentation results of the Mouse hematopoietic stem cells in Fig. 9 show that the proposed segmentation method provides the best cell detection. The SEG score, which evaluates pixel level errors, is mainly limited due to the fact that the predicted cells in the proposed method are slightly too small as indicated in Fig. 9e. These results can even be further improved by fine-tuning the mask threshold. In addition a cell type specific fine-tuning of the seed threshold can avoid the merging cells, e.g., of the two bottom cells in Fig. 9e where the second seed is just below the threshold. Surprisingly, boundaries can be learned better than adapted borders for some cell types in diverse data sets.

4.4.3 Fluo-N3DH-CE

For the segmentation of the 3D data set Fluo-N3DH-CE, we do not apply the suggested splitting of cells that are detected as merged. This enables a better comparison of the methods since the almost binary predictions of the other methods do not allow such a simple splitting post-processing. In addition to the 3D nature of this data set, the low signal-to-noise-ratio and the use of only 3 slices of that cell type in the training set makes the segmentation difficult.

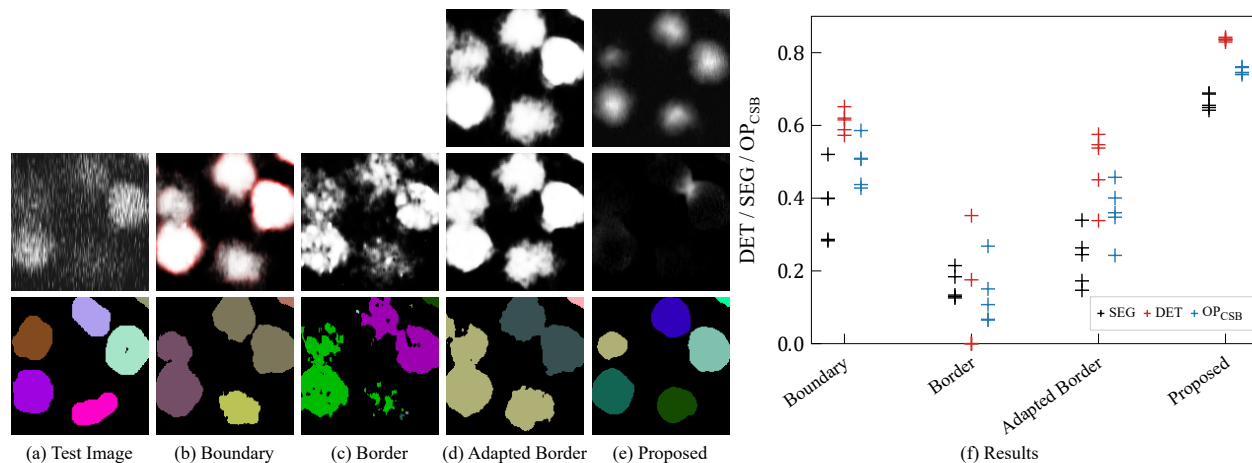


Figure 10: Segmentation results on the Fluo-N3DH-CE test set using the CTC training set. Shown are raw predictions and segmentations of a $140 \text{ px} \times 140 \text{ px}$ test image crop (a-e). For multi-channel outputs, the boundary/border prediction is visualized in red and the cell/seed channel in white. For comparison purposes, the predictions of a method’s median OP_{CSB} model are shown (b-e). The plot on the right shows the results on the test set (f). Note that this data set is a 3D data set and the wrong merging of cells can result from any of the slices a cell appears.

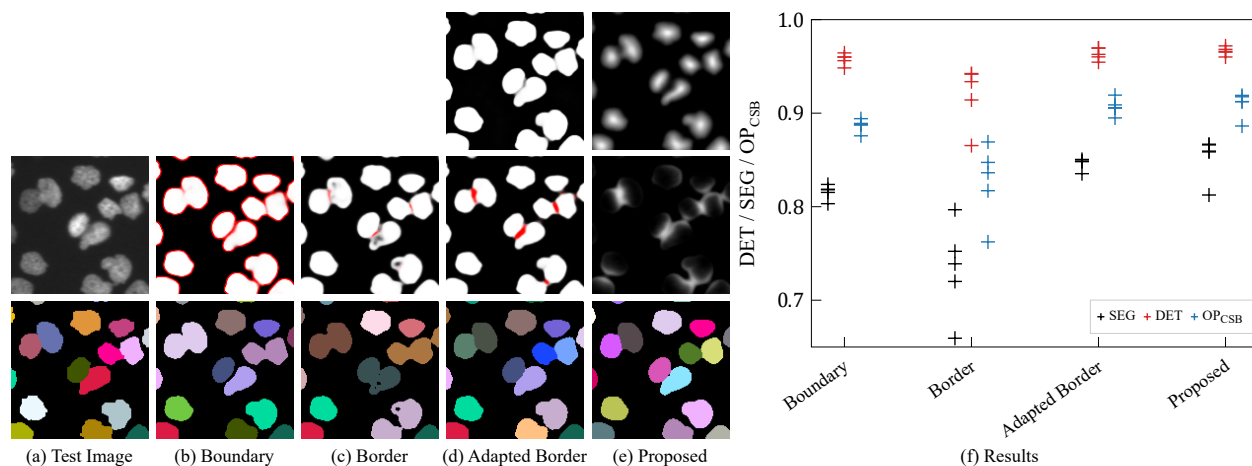


Figure 11: Segmentation results on the Fluo-N2DL-HeLa test set using the CTC training set. Shown are raw predictions and segmentations of a $140 \text{ px} \times 140 \text{ px}$ test image crop (a-e). For multi-channel outputs, the boundary/border prediction is visualized in red and the cell/seed channel in white. For comparison purposes, the predictions of a method’s median OP_{CSB} model are shown (b-e). The plot on the right shows the results on the test set (f).

Again, the proposed method shows the best results whereas boundaries are often not closed resulting in merged cells as shown in Fig. 10. Borders and adapted borders do not appear anymore and cannot be used to split cells. Especially in late frames after many cell divisions, the boundary and border segmentation method break and predict only a few very large objects.

4.4.4 Fluo-N2DL-HeLa

HeLa cells provide the largest quantity of cells from a specific cell type in the training set. Hence, relatively much HeLa border information is available in the training process resulting in the methods performing more similar, as shown in Fig. 11. However, the proposed method performs best. We assume this could be due to the possibly erroneous ST HeLa data used for training and the robustness of the method to annotation errors (see Fig. 4). The outlier in the proposed method performs consistently worst for all cell types.

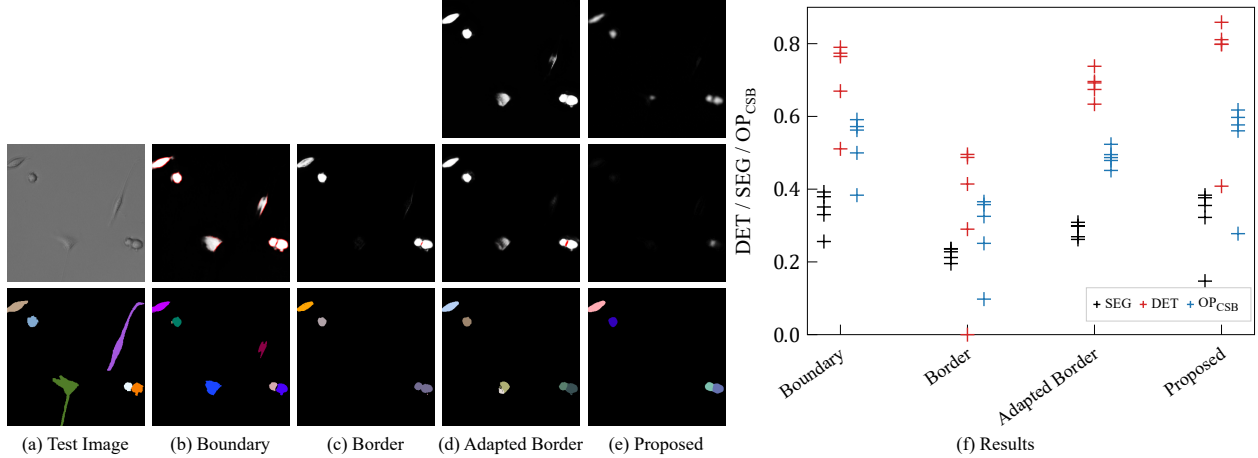


Figure 12: Segmentation results on the BF-C2DL-MuSC test set using the CTC training set. Shown are raw predictions and segmentations of a $360 \text{ px} \times 360 \text{ px}$ test image crop (a-e). For multi-channel outputs, the boundary/border prediction is visualized in red and the cell/seed channel in white. For comparison purposes, the predictions of a method’s median OP_{CSB} model are shown (b-e). The plot on the right shows the results on the test set (f).

4.4.5 BF-C2DL-MuSC

Mouse muscle stem cells are difficult to segment since they change their shape from small roundish objects to elongated objects. Both cell states are shown in Fig. 12. The boundary method handles elongated cells better. However, the proposed method provides a better detection of the small touching roundish cells resulting in the best DET and OP_{CSB} scores of all compared methods. The segmentation problem of the elongated cells can be solved using the training data of both BF-C2DL-MuSC training data subsets. This is shown in the next section.

4.5 Cell Tracking Challenge

For our submission to the 5th IEEE ISBI 2020 Cell Tracking Challenge (team KIT-Sch-GE), we combined our segmentation method with our adapted tracking approach. We selected a segmentation training data set similar to Section 3. The data set consists of 997 crops of size $256 \text{ px} \times 256 \text{ px}$ of carefully selected Cell Tracking Challenge data, CBIA HL60 cell line data [31], BBBC038 drosophila images [4], and generated semi-synthetic data [32, 33]. A more detailed description of the data set, and pre- and post-processing parameters can be found on the challenge website. The single segmentation model used for our submission was selected manually out of three trained models. In contrast to the Fluo-N3DH-CE experiment shown before, we applied the in Section 2 mentioned splitting of 3D objects to that data set, i.e., merged cells are split if their volume is bigger than $\frac{4}{3}$ times the mean object volume at that time point. Therefore, the seed extraction threshold is increased till multiple seeds are found.

For the tracking, we fixed the following parameters for all data sets: $\Delta t = 3$, $\alpha = 0.5$, $\beta = 1.2$ and $\gamma = 2 \cdot \sqrt[3]{V_{t_{last}}^s}$ with the number of image dimensions $D \in \{2, 3\}$. The ROI size is set to $150 \text{ px} \times 150 \text{ px}$ for all 2D data sets, to $60 \text{ px} \times 60 \text{ px} \times 60 \text{ px}$ for the data sets Fluo-N3DL-TRIF and Fluo-N3DL-TRIC, and to $100 \text{ px} \times 100 \text{ px} \times 100 \text{ px}$ for the other 3D data sets. For the data sets Fluo-N3DL-TRIF and Fluo-N3DL-TRIC, tracks are initialized only for the marked cells. Furthermore, frames without any tracked object are replaced by the tracking result of the temporally closest frame.

4.5.1 Cell Segmentation Benchmark

In the Cell Segmentation Benchmark, we achieved eight top three rankings, including two first places, and three fourth places, all of them with the same model (see Table 1). The performances of the highlighted data sets with no or almost no training data used imply a good utilization of training data and a good generalization ability of our model. A comparison of the scores for the data set BF-C2DL-MuSC on the CSB benchmark and the previous experiment in Fig. 12 shows an improved performance. We assume this is due to the larger amount of elongated cells in the training

Table 1: Cell Tracking Benchmark and Cell Segmentation Benchmark results. Top 3 rankings in the overall performances OP_{CSB} and OP_{CTB} are written in bold. The latest Cell Tracking Benchmark and Cell Segmentation Benchmark leaderboards are available on the Cell Tracking Challenge website.

Data Set	SEG	DET	TRA	OP_{CSB}	OP_{CTB}	Ranking OP_{CSB}	Ranking OP_{CTB}
BF-C2DL-HSC	0.750	0.974	0.929	0.862	0.840	2nd	3rd
BF-C2DL-MuSC	0.702	0.977	0.967	0.839	0.835	1st	1st
Fluo-C3DH-H157 [†]	0.789	0.949	0.948	0.869	0.869	4th	4th
Fluo-C3DL-MDA231^{††}	0.616	0.851	0.820	0.733	0.718	3rd	3rd
Fluo-N2DH-GOWT1	0.828	0.950	0.949	0.889	0.889	14th	12th
Fluo-N2DL-HeLa	0.895	0.992	0.989	0.944	0.942	3rd	3rd
Fluo-N3DH-CE^{††}	0.729	0.930	0.886	0.830	0.808	1st	1st
Fluo-N3DH-CHO	0.871	0.945	0.948	0.908	0.909	3rd	3rd
Fluo-N3DL-DRO	0.562	0.761	-	0.661	-	4th	-
Fluo-N3DL-TRIC[†]	0.821 / 0.766*	0.961	0.809	0.891	0.787	2nd	2nd
Fluo-N3DL-TRIF[†]	0.601 / 0.573*	0.926	0.788	0.763	0.680	3rd	3rd
Fluo-N2DH-SIM+	0.800	0.949	0.945	0.875	0.873	9th	7th
Fluo-N3DH-SIM+	0.668	0.937	0.933	0.802	0.800	4th	2nd

[†] No data of that cell type used to train the segmentation model.

^{††} ≤ 5 slices of that cell type used to train the segmentation model.

* Two scores for each benchmark (CSB/CTB) depending on the selection method of in the 1st frame specified cells.

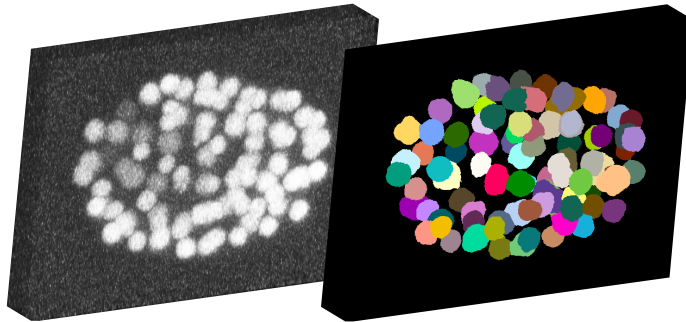


Figure 13: Exemplary segmentation result of the Fluo-N3DH-CE challenge data. The maximum intensity projection of the raw data (left) and of the segmentation result (right) show that cells can be segmented well even on this very challenging data set.

data. Furthermore, the results show that our proposed 2D segmentation with 3D post-processing approach performs well on 3D data. An exemplary segmentation result is shown in Fig. 13.

4.5.2 Cell Tracking Benchmark

In the Cell Tracking Benchmark, we achieved nine top three rankings, including two first places, and a fourth place (see Table 1). Exemplarily, some tracking results of our approach are shown in Fig. 14. Some tracks show jumps, visible as long straight lines, possibly due to some remaining linking errors in our adapted tracking approach. However, none of the competing tracking approaches yields perfect tracking results for all cells. The multiple top performances in the Cell Tracking Benchmark show that our tracking approach, which combines a movement estimation and a graph-based matching strategy, belongs to the best performing approaches.

4.6 Discussion

For the segmentation of touching cells in single cell type data sets with many touching samples, (adapted) borders can be learned well and the segmentation measures are mainly limited due to annotation errors or single pixel differences.

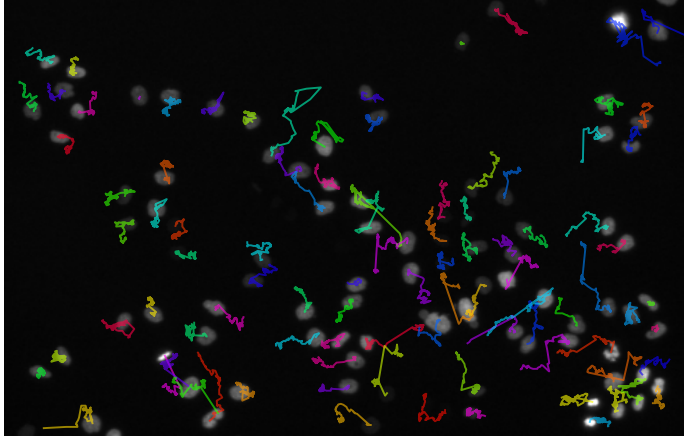


Figure 14: Exemplary tracking results on the Fluo-N2DL-HeLa challenge data. The first raw image is overlaid with the tracks starting in the first frame. For better visibility, tracks starting in later frames are excluded.

Our proposed combination of cell distances and novel neighbor distances also performs well but shows some additional splits, which would need to be corrected in a more sophisticated post-processing.

In case of segmenting multiple cell types with a single model or segmenting cell types with few touching samples, our proposed segmentation method outperforms the boundary and border methods. This is due to the fact that the neighbor distances enable our method to also learn from close cells which results in additional information in the training process. The results on the BBBC039v1 data set show, that there is only a small difference for the proposed method trained BBBC039v1 data and trained on data without BBBC039v1 samples. In contrast, the boundary and border methods drop in segmentation quality.

We want to emphasize that the seed and the mask thresholds in the post-processing can be adjusted for each cell type and for each trained model separately. This improves the segmentation results shown in Fig. 7 - Fig. 12. The discrete boundary and border methods do not allow to do so since the needed sigmoid or softmax activation functions prevent a major fine-tuning of the post-processing. However, to allow a better comparison, we fixed the post-processing parameters of our proposed method.

Our successful participation in the Cell Segmentation Benchmark and the Cell Tracking Benchmark show that our proposed tracking by detection method yields excellent results in cell segmentation and cell tracking. Especially the success on data sets with only little or very sparse annotated training data, i.e., data with only very few cells in a frame annotated, shows the advantages of our method.

5 Conclusion

The segmentation and tracking of touching and dividing cells of different types is a challenging task. In this work, a new cell segmentation method using a combination of cell distances and neighbor distances is proposed. The segmentation method utilizes information from touching and close cells in the training process. Therefore, it shows an improved generalization ability to in the training data set absent or under-represented cell types compared to boundary and border prediction methods. This advantage enables to segment even cell types with no annotated training data available. Our success in the Cell Segmentation Benchmark emphasizes the strengths of our segmentation method. Our adapted tracking algorithm, which uses a movement estimation with a graph-based matching strategy, can handle cell divisions and missing segmentation masks for short time periods. The combination of the tracking with our proposed segmentation method resulted in top performances at the Cell Tracking Benchmark.

As future research, we plan to further improve the segmentation performance using a larger and on ImageNet pre-trained encoder, test-time augmentation [34], and the synthetic generation of new training samples[15]. A long-term goal is to develop a user-friendly-software for the segmentation and tracking of a large variety of cell types using a well-trained segmentation model. Including tunable post-processing parameters facilitates an adaptation of the cell and neighbor distances to new data.

Acknowledgment

The authors would like to thank Andreas Bartschat for proofreading, the organizers of the Cell Tracking Challenge, and all data set providers.

Author Contributions

TS designed and implemented the segmentation. KL designed and implemented the tracking. MB and TS developed the idea of the neighbor distances. RM supervised the project. All authors discussed the results and commented on the paper. TS and KL are the main authors of the paper.

References

- [1] R. K. Chhetri, F. Amat, Y. Wan, B. Höckendorf, W. C. Lemon, and P. J. Keller, “Whole-animal functional and developmental imaging with isotropic spatial resolution,” *Nat. Methods*, vol. 12, pp. 1171–1178, 2015, DOI: 10.1038/nmeth.3632.
- [2] A. Y. Kobitski, J. C. Otte, M. Takamiya, B. Schäfer, J. Mertes, J. Stegmaier, S. Rastegar, F. Rindone, V. Hartmann, R. Stotzka, A. Garcia, J. van Wezel, R. Mikut, U. Strähle, and G. U. Nienhaus, “An ensemble-averaged, cell density-based digital model of zebrafish embryo development derived from light-sheet microscopy data with single-cell resolution,” *Sci. Rep.*, vol. 5, no. 8601, pp. 1–10, 2015, DOI: 10.1038/srep08601.
- [3] K. Khairy and P. J. Keller, “Reconstructing embryonic development,” *Genesis*, vol. 49, pp. 488–513, 2011, DOI: 10.1002/dvg.20698.
- [4] J. C. Caicedo, A. Goodman, K. W. Karhohs, B. A. Cimini, J. Ackerman, M. Haghghi, C. Heng, T. Becker, M. Doan, C. McQuin, M. Rohban, S. Sing, and A. E. Carpenter, “Nucleus segmentation across imaging experiments: The 2018 Data Science Bowl,” *Nat. Methods*, vol. 16, pp. 1247–1253, 2019, DOI: 10.1038/s41592-019-0612-7.
- [5] B. Schott, M. Traub, C. Schlagenhauf, M. Takamiya, T. Anritter, A. Bartschat, K. Löffler, D. Blessing, J. C. Otte, A. Y. Kobitski, G. U. Nienhaus, U. Strähle, R. Mikut, and J. Stegmaier, “EmbryoMiner: A new framework for interactive knowledge discovery in large-scale cell tracking data of developing embryos,” *PLOS Comput. Biol.*, vol. 14, no. 4, pp. 1–18, 2018, DOI: 10.1371/journal.pcbi.1006128.
- [6] C. Wolff, J.-Y. Tinevez, T. Pietzsch, E. Stamataki, B. Harich, L. Guignard, S. Preibisch, S. Shorte, P. J. Keller, P. Tomancak, and A. Pavlopoulos, “Multi-view light-sheet imaging and tracking with the MaMuT software reveals the cell lineage of a direct developing arthropod limb,” *eLife*, vol. 7, p. e34410, 2018, DOI: 10.7554/eLife.34410.
- [7] V. Ulman, M. Maška, K. E. Magnusson, O. Ronneberger, C. Haubold, N. Harder, P. Matula, P. Matula, D. Svoboda, M. Radojevic *et al.*, “An objective comparison of cell-tracking algorithms,” *Nat. Methods*, vol. 14, pp. 1141–1152, 2017, DOI: 10.1038/nmeth.4473.
- [8] M. Maška, V. Ulman, D. Svoboda, P. Matula, P. Matula, C. Eder, A. Urbiola, T. España, S. Venkatesan, D. M. Balak, P. Karas, T. Bolcková, M. Štreitová, C. Carthel, S. Coraluppi, N. Harder, K. Rohr, K. E. G. Magnusson, J. Jaldén, H. M. Blau, O. Dzyubachyk, P. Křížek, G. M. Hagen, D. Pastor-Escuredo, D. Jimenez-Carretero, M. J. Ledesma-Carbayo, A. Muñoz-Barrutia, E. Meijering, M. Kozubek, and C. Ortiz-de Solorzano, “A benchmark for comparison of cell tracking algorithms,” *Bioinformatics*, vol. 30, no. 11, pp. 1609–1617, 2014, DOI: 10.1093/bioinformatics/btu080.
- [9] J. Stegmaier, J. C. Otte, A. Kobitski, A. Bartschat, A. Garcia, G. U. Nienhaus, U. Strähle, and R. Mikut, “Fast segmentation of stained nuclei in terabyte-scale, time resolved 3D microscopy image stacks,” *PLOS ONE*, vol. 9, no. 2, pp. 1–11, 2014, DOI: 10.1371/journal.pone.0090036.
- [10] T. Scherr, A. Bartschat, M. Reischl, J. Stegmaier, and R. Mikut, “Best practices in deep learning-based segmentation of microscopy images,” in *Proceedings 28. Workshop Computational Intelligence, Dortmund, Germany*, 2018, pp. 175–195, DOI: 10.5445/IR/1000087734.
- [11] F. A. G. Peña, P. D. M. Fernandez, P. T. Tarr, T. I. Ren, E. M. Meyerowitz, and A. Cunha. (2019) “J regularization improves imbalanced multiclass segmentation.” arXiv: 1910.09783.
- [12] X. Li, Y. Wang, Q. Tang, Z. Fan, and J. Yu, “Dual U-Net for the segmentation of overlapping glioma nuclei,” *IEEE Access*, vol. 7, pp. 84 040–84 052, 2019, DOI: 10.1109/ACCESS.2019.2924744.

- [13] J. Li, Z. Hu, and S. Yang, “Accurate nuclear segmentation with center vector encoding,” in *Information Processing in Medical Imaging*. Springer International Publishing, 2019, pp. 394–404, DOI: 10.1007/978-3-030-20351-1_30.
- [14] S. Graham, Q. D. Vu, S. E. A. Raza, A. Azam, Y. W. Tsang, J. T. Kwak, and N. Rajpoot, “Hover-Net: Simultaneous segmentation and classification of nuclei in multi-tissue histology images,” *Med. Image Anal.*, vol. 58, p. 101563, 2019, DOI: 10.1016/j.media.2019.101563.
- [15] R. Hollandi, A. Szkalisity, T. Toth, E. Tasnadi, C. Molnar, B. Mathe, I. Grexa, J. Molnar, A. Balind, M. Gorbe, M. Kovacs, E. Migh, A. Goodman, T. Balassa, K. Koos, W. Wang, N. Bara, F. Kovacs, L. Paavolainen, T. Danko, A. Kriston, A. E. Carpenter, K. Smith, and P. Horvath. (2019) “A deep learning framework for nucleus segmentation using image style transfer.” bioRxiv, DOI: 10.1101/580605.
- [16] G. Ciaparrone, F. L. Sánchez, S. Tabik, L. Troiano, R. Tagliaferri, and F. Herrera, “Deep learning in video multi-object tracking: A survey,” *Neurocomputing*, vol. 381, pp. 61 – 88, 2020, DOI: 10.1016/j.neucom.2019.11.023.
- [17] R. Yao, G. Lin, S. Xia, J. Zhao, and Y. Zhou. (2019) “Video object segmentation and tracking: A survey.” arXiv: 1904.09172.
- [18] C. Payer, D. Štern, M. Feiner, H. Bischof, and M. Urschler, “Segmenting and tracking cell instances with cosine embeddings and recurrent hourglass networks,” *Med. Image Anal.*, vol. 57, pp. 106–119, 2019, DOI: 10.1016/j.media.2019.06.015.
- [19] T. He, H. Mao, J. Guo, and Z. Yi, “Cell tracking using deep neural networks with multi-task learning,” *Image Vision Comput.*, vol. 60, pp. 142–153, 2017, DOI: 10.1016/j.imavis.2016.11.010.
- [20] K. E. G. Magnusson, J. Jalden, P. M. Gilbert, and H. M. Blau, “Global linking of cell tracks using the Viterbi algorithm,” *IEEE Trans. Med. Imag.*, vol. 34, no. 4, pp. 911–929, 2015, DOI: 10.1109/TMI.2014.2370951.
- [21] P. Dendorfer, H. Rezatofighi, A. Milan, J. Shi, D. Cremers, I. Reid, S. Roth, K. Schindler, and L. Leal-Taixe. (2019) “CVPR19 tracking and detection challenge: How crowded can it get?” arXiv: 1906.04567.
- [22] J. Pont-Tuset, F. Perazzi, S. Caelles, P. Arbeláez, A. Sorkine-Hornung, and L. Van Gool. (2018) “The 2017 DAVIS challenge on video object segmentation.” arXiv: 1704.00675.
- [23] N. Xu, L. Yang, Y. Fan, D. Yue, Y. Liang, J. Yang, and T. Huang. (2018) “YouTube-VOS: A large-scale video object segmentation benchmark.” arXiv: 1904.09172.
- [24] T. Sixta, J. Cao, J. Seebach, H. Schnittler, and B. Flach, “Coupling cell detection and tracking by temporal feedback,” *Machine Vision and Applications*, vol. 31, no. 4, p. 24, 2020.
- [25] V. Ljosa, K. L. Sokolnicki, and A. E. Carpenter, “Annotated high-throughput microscopy image sets for validation,” *Nat. Methods*, vol. 9, p. 637, 2012, DOI: 10.1038/nmeth.2083.
- [26] O. Ronneberger, P. Fischer, and T. Brox, “U-Net: Convolutional networks for biomedical image segmentation,” in *MICCAI 2015*. Springer International Publishing, 2015, pp. 234–241.
- [27] D. Kingma and J. Ba, “Adam: A method for stochastic optimization,” in *ICLRCR*, 2014.
- [28] D. Padfield, J. Rittscher, and B. Roysam, “Coupled minimum-cost flow cell tracking for high-throughput quantitative analysis,” *Med. Image Anal.*, vol. 15, no. 4, pp. 650 – 668, 2011, DOI: 10.1016/j.media.2010.07.006.
- [29] P. Matula, M. Maška, D. V. Sorokin, P. Matula, C. Ortiz-de Solórzano, and M. Kozubek, “Cell tracking accuracy measurement based on comparison of acyclic oriented graphs,” *PLOS ONE*, vol. 10, no. 12, pp. 1–19, 2015, DOI: 10.1371/journal.pone.0144959.
- [30] C. McQuin, A. Goodman, V. Chernyshev, L. Kamensky, B. A. Cimini, K. W. Karhohs, M. Doan, L. Ding, S. M. Rafelski, D. Thirstrup, W. Wiegraebe, S. Singh, T. Becker, J. C. Caicedo, and A. E. Carpenter, “Cell-Profiler 3.0: Next-generation image processing for biology,” *PLOS Biol.*, vol. 16, no. 7, pp. 1–17, 2018, DOI: 10.1371/journal.pbio.2005970.
- [31] D. Svoboda, M. Kozubek, and S. Stejskal, “Generation of digital phantoms of cell nuclei and simulation of image formation in 3d image cytometry,” *Cytom. Part A*, vol. 75A, no. 6, pp. 494–509, 2009, DOI: 10.1002/cyto.a.20714.
- [32] J. Stegmaier, “New methods to improve large-scale microscopy image analysis with prior knowledge and uncertainty,” Ph.D. dissertation, ME, KIT, Karlsruhe, GER, 2017, DOI: 10.5445/KSP/1000060221.
- [33] J. Stegmaier, J. Arz, B. Schott, J. C. Otte, A. Kobitski, G. U. Nienhaus, U. Strähle, P. Sanders, and R. Mikut, “Generating semi-synthetic validation benchmarks for embryomics,” in *2016 IEEE ISBI*, 2016, pp. 684–688, DOI: 10.1109/ISBI.2016.7493359.
- [34] N. Moshkov, B. Mathe, A. Kertesz-Farkas, R. Hollandi, and P. Horvath, “Test-time augmentation for deep learning-based cell segmentation on microscopy images,” *Sci. Rep.*, vol. 10, no. 5068, 2020, DOI: 10.1038/s41598-020-61808-3.